

Influence of acoustic streaming on ultrasonic particle manipulation in a 100-well ring-transducer microplate

This content has been downloaded from IOPscience. Please scroll down to see the full text.

2013 J. Micromech. Microeng. 23 035008

(<http://iopscience.iop.org/0960-1317/23/3/035008>)

View [the table of contents for this issue](#), or go to the [journal homepage](#) for more

Download details:

IP Address: 130.237.35.39

This content was downloaded on 18/09/2014 at 14:31

Please note that [terms and conditions apply](#).

Influence of acoustic streaming on ultrasonic particle manipulation in a 100-well ring-transducer microplate

Mathias Ohlin¹, Athanasia E Christakou¹, Thomas Frisk¹,
Björn Önfelt^{1,2} and Martin Wiklund¹

¹ Department of Applied Physics, Royal Institute of Technology, KTH-Albanova, SE-106 91 Stockholm, Sweden

² Department of Microbiology, Tumor and Cell Biology, Karolinska Institutet, SE-171 77, Stockholm, Sweden

E-mail: mathias.ohlin@bio.kth.se

Received 12 September 2012, in final form 12 December 2012

Published 25 January 2013

Online at stacks.iop.org/JMM/23/035008

Abstract

We characterize and quantify the performance of ultrasonic particle aggregation and positioning in a 100-well microplate. We analyze the result when operating a planar ultrasonic ring transducer at different single actuation frequencies in the range 2.20–2.40 MHz, and compare with the result obtained from different schemes of frequency-modulated actuation. Compared to our previously used wedge transducer design, the ring transducer has a larger contact area facing the microplate, resulting in lower temperature increase for a given actuation voltage. Furthermore, we analyze the dynamics of acoustic streaming occurring simultaneously with the particle trapping in the wells of the microplate, and we define an adaptive ultrasonic actuation scheme for optimizing both efficiency and robustness of the method. The device is designed as a tool for ultrasound-mediated cell aggregation and positioning. This is a method for high-resolution optical characterization of time-dependent cellular processes at the level of single cells. In this paper, we demonstrate how to operate our device in order to optimize the scanning time of 3D confocal microscopy with the aim to perform high-resolution time-lapse imaging of cells or cell–cell interactions in a highly parallel manner.

(Some figures may appear in colour only in the online journal)

1. Introduction

Standing wave ultrasonic manipulation of cells or other μm -sized particles has long been used as a tool for enhancing biotechnology applications, e.g. for clumping or filtering of particles [1]. Recently, the method has gained increased attention when applied to lab-on-a-chip devices [2]. For particle separation or migration purposes, the method is referred to as acoustophoresis [3–5], while for aggregation and positioning purposes the method is often called acoustic trapping [6]. Common for all purposes is to use ultrasonic standing waves established inside a microchannel or similar fluid-filled micro-compartment for driving cells or particles into the pressure nodes of the standing wave [7]. We have

previously demonstrated how to form cell aggregates in parallel by frequency-modulated ultrasound inside the wells of a 100-well microplate actuated with a wedge transducer [8], and how to suppress acoustic streaming inside the wells of the microplate [9, 10]. Although the method has been used successfully for studying the interaction between individual natural killer (NK) cells and cancer cells [11, 12], the method is currently limited by two factors. (1) The assembly of the cell aggregates is slow (of the order of minutes) and (2) the robustness of the method is unsatisfactory, in particular when the device is operated at high actuation voltages. In order to address these limitations, we investigate in this paper a novel ring transducer for the acoustic actuation, which is designed to

be compatible with higher actuation voltages and frequency-modulated actuation.

Single-cell analysis is important for studying cellular heterogeneity in contrast to bulk methods where only average cell properties can be resolved [13]. In order to efficiently acquire statistically significant data, it is important that the single-cell analysis method has sufficient throughput. One good example of a method combining both single-cell resolution and fast data acquisition time is a flow cytometer. However, one limitation with a flow cytometer is that it can only perform post-screening of instant cellular properties. When dynamic properties of a cell or a cell–cell interaction are of interest, we suggest an alternative method called dynamic micro-array cytometry (DMAC). This method is similar to the dielectrophoresis-mediated and microfabrication-based dynamic array cytometer (μ -DAC) method reported by Voldman *et al* [14]. Both μ -DAC and DMAC are flow-free dynamic cytometry methods based on parallel screening of cells arranged in a two-dimensional array, e.g., by the use of a multiwell microplate [8, 11, 12, 15, 16]. For high-resolution screening purposes, it is important that the cells are accurately positioned during the full assay time. Here, contactless manipulation by ultrasonic radiation forces is an attractive method for gentle cell positioning with, if desired, minimal interference with the naturally occurring biological forces responsible for, e.g., cell adhesion and migration [17]. This is particularly important when studying the long-term behavior of motile non-adherent cells, such as NK cells and their interaction with different types of target cells [12]. We have previously used the ultrasound-mediated DMAC method for measuring the cytotoxic heterogeneity of NK cells interacting with cancer cells [12], and for characterizing the immune synapse formed between the NK cells and cancer cells [11]. In these studies, the temporal resolution of the confocal-microscopy tile scans was between 6 and 7 min. However, when faster biological processes are of interest, both the ultrasonic aggregation time and the temporal resolution of the confocal screening time need to be enhanced.

Our previously designed microdevices for ultrasonic manipulation are based on glass–silicon microchips or microplates combined with ultrasonic wedge transducers [18]. The wedge transducers have proven to be useful in practical applications [8, 11, 12, 18–20] but they cannot be driven at high voltages (>20 V) without causing significant temperature elevations in the devices [21]. In this paper, we characterize and evaluate an alternative transducer design based on a ring transducer with much larger surface contact area attached to a 100-well microplate. We quantify the positioning performance of few-particle clusters at different schemes of ultrasonic actuation (including different single frequencies, SFs, as well as frequency sweeps), and we use this information with the aim to optimize high-resolution 3D-confocal-microscopy screening of cellular clusters trapped in the microplate. Furthermore, we use particle tracking for estimating the acoustic energy density, pressure and acoustic radiation forces acting on particles and cells when the device is operated at high voltage actuation, and we investigate the dynamics of acoustic streaming and its influence on particle

aggregation and positioning. Our results can be used for implementing an adaptive ultrasonic actuation scheme for a given DMAC application, which takes into account the screening time, positioning accuracy and biocompatibility.

2. Theoretical background

Technology for ultrasonic manipulation of particles and cells utilizes the acoustic radiation force, F^{rad} , originating from the nonlinear interaction between the incident and scattered wave on the particle [22, 23]. In this section, we summarize the important equations used for estimating the energy density, pressure and forces acting on the polymer particles in our experiments. In a one-dimensional standing-wave system, where the propagation direction is parallel with the z -axis, this force, acting on a particle with radius a , is given by [7]

$$F_z^{\text{rad}} = 4\pi \Phi k a^3 E_{ac} \sin(2kz), \quad (1a)$$

where

$$\Phi = \frac{1}{3} \left[\frac{5\rho_{\text{ratio}} - 2}{2\rho_{\text{ratio}} + 1} - \kappa_{\text{ratio}} \right], \quad (1b)$$

$$\kappa_{\text{ratio}} = \frac{\rho_0 c_0^2}{\rho_P c_P^2} \quad (1c)$$

and

$$E_{ac} = \frac{p_a^2}{4\rho_0 c_0^2}. \quad (1d)$$

Here, input parameters when estimating the radiation force are the sound velocities in the suspension medium (c_0) and in the particle (c_P), respectively, and the acoustic contrast factor (Φ) defined by (1b). Φ is dependent on the density ratio between the particle and the suspension medium ($\rho_{\text{ratio}} = \rho_P/\rho_0$) and the compressibility ratio between the particle and the suspension medium ($\kappa_{\text{ratio}} = \kappa_P/\kappa_0$) where the latter is defined by equation (1c). The expression for the radiation force (1a) also contains E_{ac} which is the acoustic energy density defined by (1d), where p_a is the acoustic pressure amplitude. Typically, p_a is proportional to the applied voltage over the transducer [24]. Furthermore, the wavenumber, k , in (1a) is proportional to the applied frequency, f , via $k = 2\pi f/c_0$. Of all the parameters in equations (1a)–(1d), it is the acoustic pressure amplitude, p_a , and the acoustic energy density, E_{ac} , that are the most difficult to measure or estimate directly. These field parameters must be known in order to calculate the acoustic radiation force, F^{rad} .

A common indirect method for estimating F^{rad} , E_{ac} and p_a is to use particle tracking for measuring the speed of a particle migrating toward the pressure node of the acoustic standing wave [25]. This speed, v_P , is defined by balancing the acoustic radiation force with the viscous Stokes drag force (in a medium with dynamic viscosity η_0) resulting in [7]

$$v_P(z) = \frac{\pi a^2 f p_a^2}{3\rho_0 c_0^3 \eta_0} \Phi \sin(2kz), \quad (2a)$$

with the maximum speed given by

$$v_P^{\text{max}} = \frac{\pi a^2 f p_a^2}{3\rho_0 c_0^3 \eta_0} \Phi. \quad (2b)$$

Furthermore, the maximum energy density and maximum radiation force can be written as

$$E_{ac}^{max} = \frac{3\eta_0 v_p^{max}}{2\Phi k a^2} \quad (3a)$$

and

$$F_z^{max,rad} = 6\eta_0 \pi a v_p^{max}. \quad (3b)$$

Finally, the maximum acoustic pressure amplitude can be estimated using the maximum energy density as follows [25]:

$$p_a^{max} = 2\sqrt{\rho_0 c_0^2 E_{ac}^{max}}. \quad (4)$$

In a simple one-dimensional half-wave wide fluid cavity, this maximum speed, v_p^{max} , is achieved just in between the reflecting wall of the cavity and the pressure node in the center of the cavity, i.e. at the approximate distance $\lambda/8$ from the trapping location in the pressure node (where λ is the acoustic wavelength in the fluid).

3. Materials and methods

3.1. Ultrasound ring-transducer and 100-well microplate

Our device, consisting of a 100-well microplate and an ultrasound transducer, is shown schematically in figure 1. The design of the microplate is similar to the glass–silicon chip described in [8], but in this paper we used slightly larger wells ($350 \mu\text{m}$ width and height) for improving the loading capacity. In brief, the microplate consists of a $22 \times 22 \times 0.175 \text{ mm}^3$ glass bottom layer which is anodically bonded to a $22 \times 22 \times 0.3 \text{ mm}^3$ silicon top layer. In the center of the silicon layer, there are 10×10 wells with slightly rounded walls (see figure 3) fabricated by dry-etching technology. Furthermore, the well-to-well distance is 0.1 mm and the well depth is 0.3 mm , corresponding to a well volume of 35 nL . A polydimethylsiloxane (PDMS) frame is bonded around the wells on the top layer (cf ‘6’ in figure 1) to increase the sample volume capacity. This adds another $50 \mu\text{L}$ on top of the $3.5 \mu\text{L}$ volume of the 100 wells. In order to prevent evaporation of the fluid sample, a cover glass is placed on top of the PDMS frame.

The microplate is fixated in the transducer between the ring-shaped lead zirconate titanate (PZT) piezo crystal (Pz-26, Ferroperm, Denmark) and the spacer and held into position by the variable spring-loaded holder. In addition, a thin layer of oil (Immersol 518 F, Zeiss, Germany) is applied between the bottom surface of the microplate and the piezo crystal for the coupling of the ultrasound into the microplate. Optical access is available on both sides of the device making it compatible with high-resolution epi- and trans-illumination microscopy [26]. The ring-shaped PZT piezo crystal (38.3 mm in diameter, 0.86 mm thick with a 8 mm diameter center hole) is used for acoustic actuation of the microplate in the frequency range $2.20\text{--}2.46 \text{ MHz}$. The choice of the ring-shaped geometry of the piezo crystal was based on maximizing the surface contact area between the piezo and the microplate without compromising the optical access of the wells (i.e. visual access is provided through the hole). The piezo crystal is actuated using peak-to-peak voltages (U_{pp}) ranging from 50 V up to

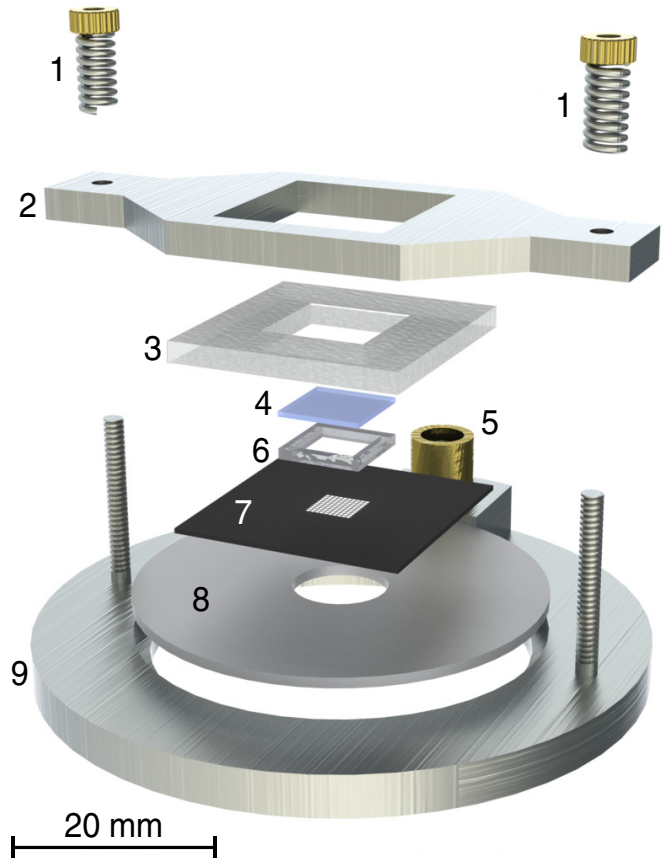


Figure 1. Illustration of the device (ultrasound ring transducer and 100-well microplate). (1) Springs, (2) aluminum clip, (3) polymethyl methacrylate (PMMA) spacer, (4) cover glass, (5) micro coaxial (MCX) connector, (6) PDMS frame, (7) 100-well microplate, (8) ring-shaped PZT piezo crystal, (9) aluminum baseplate.

210 V . The temperature is measured directly on the piezo crystal surface using a type-T cement-on surface thermocouple (CO1-T-72 INCH, Omega Engineering, USA), but also in the fluid and in the ambient air close to the device using a type-T thermocouple microprobe (MT-4, Physitemp Instruments, USA). The ambient air was measured in order to compensate for different initial temperatures between repetitions of the same experiments caused by room temperature drifts.

3.2. Tracer particles and sample loading

In contrast to the proof-of-concept experiments in [8], we used in this paper polystyrene particles instead of cells. The reason for this choice is because of the well-known and uniform material properties of polystyrene, which allowed us to quantify the acoustic energy density, acoustic radiation forces and acoustic streaming inside the wells of the microplate. Two types of tracer particles were used. The acoustic streaming was visualized by red-fluorescent $1 \mu\text{m}$ sized polystyrene particles (Fluoro-Max, Fisher Scientific, USA) and the acoustic trapping by $10 \mu\text{m}$ sized green-fluorescent polystyrene particles (Fluoro-Max, Fisher Scientific, USA). Both particle types were mixed together with Milli-Q water and 0.01% TWEEN-20 (663684B, VWR, France). The stock

solutions were diluted 1:50 and 1:200 for the 1 μm sized particles and 10 μm sized particles, respectively, resulting in particle concentrations of 3.6×10^8 and $9.1 \times 10^4 \text{ mL}^{-1}$ (for the 1 and 10 μm particles, respectively). Finally, the microplate was loaded with 20 μL of the 10 μm particle suspension and 30 μL of the 1 μm particle suspension making it possible to visualize the acoustic streaming and the acoustic trapping simultaneously. This is possible because of the size dependence of the relevant forces; the 10 μm sized tracer particles are less influenced by the acoustic streaming, while the 1 μm sized tracer particles are less influenced by the acoustic radiation forces at the utilized frequency range (approx. 2 MHz) [27].

3.3. Microscopy and image analysis

For the experiments, two different types of microscopy systems were used. An inverted laser-scanning confocal microscope (Zeiss LSM 5 Pascal, Zeiss, Germany) with objective (2.5 \times /0.07, Zeiss, Germany), and an inverted bright-field microscope (Axiovert 40 CFL, Zeiss, Germany) with objective (20 \times /0.30, Zeiss, Germany). Hence, the two systems allow for both high-resolution (single-well) imaging and wide-field-of-view (100-well) imaging. For all images, the microscope was focused for imaging sharply at the bottom of the wells where the particles were typically trapped. A CCD camera (AxioCam HSC, Zeiss, Germany) was used for recording of videos, which were processed and converted into series of images using AxioVision Rel. 4.8 software. The images were then analyzed with both Matlab and the free video analysis tool Tracker Rel. 4.62 [28], allowing for acoustic trapping and streaming characterization as well as single particle tracking of the 10 μm tracer particles. To analyze the acoustic streaming, the images were converted into binary images and then analyzed by the use of micro-particle image velocimetry (μPIV) utilizing the free-particle image velocimetry toolbox for Matlab [29].

3.4. Experimental procedure

The resonances of the ring transducer were characterized by admittance analysis using an impedance analyzer (Z-Check 16777k, Sinephase, Austria). The transducer actuation was performed by the use of a signal generator (DS345, Stanford, USA) together with a radio-frequency (RF) amplifier (75A250, Amplifier Research, USA). Moreover, the average power consumption of the ring transducer was measured using a directional coupler (DC2600A, Amplifier Research, USA) together with a RF power sensor (PMM 6630, Narda Safety Test Solutions, Italy) connected between the ring transducer and the RF amplifier. The signal was adjusted with a 10 \times attenuator probe (PM8927A, Philips, the Netherlands) and monitored on an oscilloscope (TDS7104, Tektronix, USA). The temperatures were measured with a precision measuring instrument (P655-Log, Dostmann electronic, Germany) together with DE-graph (Rel. 1.3.3. software).

Three particle manipulation experiments were performed: (1) quantification of the particle aggregate positioning accuracy for different schemes of transducer actuation, (2)

quantification of acoustic energy density, acoustic radiation forces and acoustic pressure during the formation of particle aggregates and (3) measurements of the temperature, fluid volume and time dependence of the acoustic streaming and its influence on the particle manipulation. In all three experiments, the same device and tracer particles were used; see sections 3.1 and 3.2, respectively. However, the transducer voltage, U_{pp} , was different in the experiments. For the first experiment the U_{pp} was approx. 50 V compared to the second and third experiments, where the U_{pp} was typically set to a level between ~ 100 and 200 V. These voltage levels were chosen for prioritizing either positioning stability (~ 50 V) or speed of particle migration toward the trapping position (~ 100 –200 V). For the higher voltage levels, the exact value for each experiment was chosen in order to achieve a certain surface temperature on the piezo crystal, e.g. 37 $^\circ\text{C}$. Two different types of actuation schemes were implemented for the experiments, the SF and the frequency-modulation [30] (FM) modality. In this paper, the FM actuation was performed by a linear sweep around two different center frequencies: either 2.30 or 2.36 MHz, and with a bandwidth of 200 kHz and at a rate of 1 kHz. For SF actuation, nine different SFs were used: 2.20, 2.23, 2.26, 2.29, 2.30, 2.33, 2.36, 2.39 and finally 2.40 MHz. In the first experiment, we used a confocal microscope adjusted for acquiring images with a large field of view (FOV) covering all 100 wells in a single image. After the sample was loaded and the wells were filled with a uniform distribution of 10 and 1 μm tracer particles, the ultrasound was turned on using either SF or FM actuation. When the particles had reached a steady state pattern (typically within 2 min), a single confocal scan was performed (scanning time of 31 s). This procedure was repeated for each SF and for the FM yielding one image for each frequency and one for FM actuation, in total ten images. The scanned images were then analyzed and the positioning accuracy measured. The bright-field microscope was used in epi-fluorescent mode in the second and third experiments where a smaller FOV was needed for studying a single well for six repetitions at higher resolution. The CCD camera recorded videos of the acoustic trapping of 10 μm particles and streaming tracked with the 1 μm particles at a frame rate of 20 frames per second. The recorded videos underwent the same image processing as for the scanned images from the confocal microscope and finally analyzed for quantifying the acoustic trapping and acoustic streaming. Temperatures were measured throughout the 5 min long third experiment, on the PZT piezo crystal surface and in the ambient air close to the device.

4. Results

4.1. Impedance analysis of the ring transducer

The resonance characteristics of the ring transducer driven in thickness resonance mode (see figure 1) were characterized by admittance analysis. Figure 2 shows the admittance as a function of frequency, including the calculated Q -values of the ring transducer for the different steps of manufacturing and device assembly. The admittance at resonance decreases

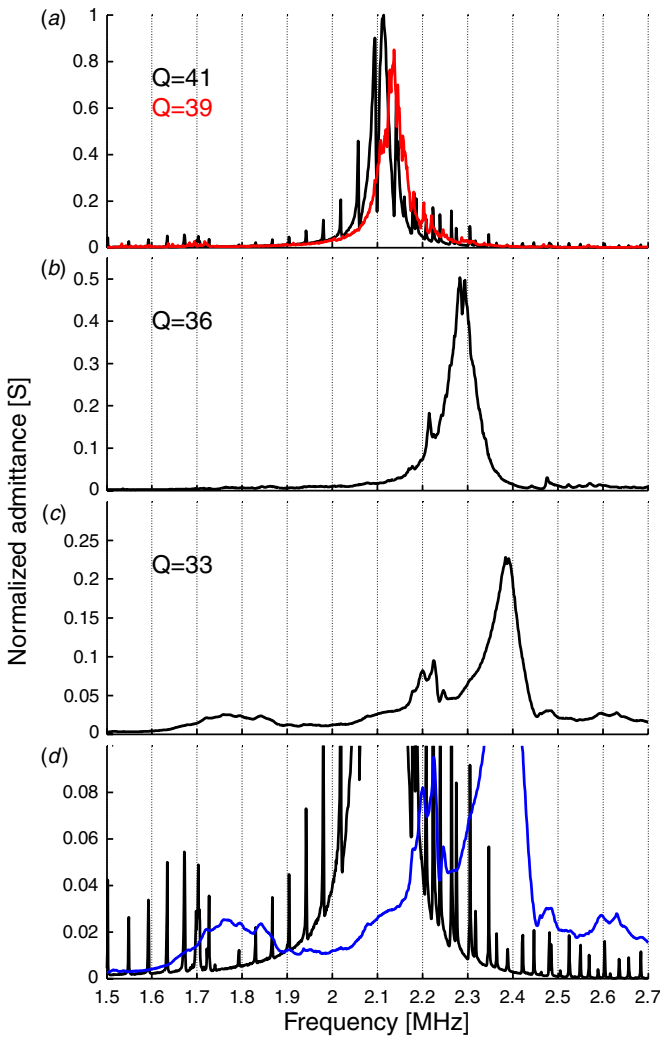


Figure 2. Admittance as a function of frequency for the ring-shaped PZT piezo crystal showing (a) the admittance scans for the PZT crystal before drilling of the center hole (black line) and after drilling (red line). (b) The admittance scan of the PZT crystal after drilling and being mounted on the baseplate (cf (9) in figure 1) using adhesive. (c) The admittance scan for the complete setup, i.e. the ultrasound transducer with the 100-well microplate installed. (d) A detailed comparison between the admittance scan for the black line in (a) and the admittance scan in (c) represented by the blue line in (d), i.e. the admittance scan before manufacturing and the final setup. All admittance scans are normalized with respect to the first admittance scan for the PZT crystal before drilling the center hole (black line in (a)).

to 23% of its initial value (the black curve in figure 2(a)) for the complete device (see figure 2(c)) and the corresponding Q -value decreases from 41 to 33. However, although the admittance at resonance decreases, there is an admittance increase for frequencies around this peak as well as the broadening of the ring-transducer frequency range as can be seen in figure 2(d). The resonance frequency is also shifted upward from 2.1 to 2.4 MHz for the complete device (see figures 2(a) and (c)). As a result, the final device has a larger usable frequency range compared with the initially undrilled PZT piezo crystal. This makes the ring transducer compatible with FM actuation using bandwidths (frequency sweeps) of

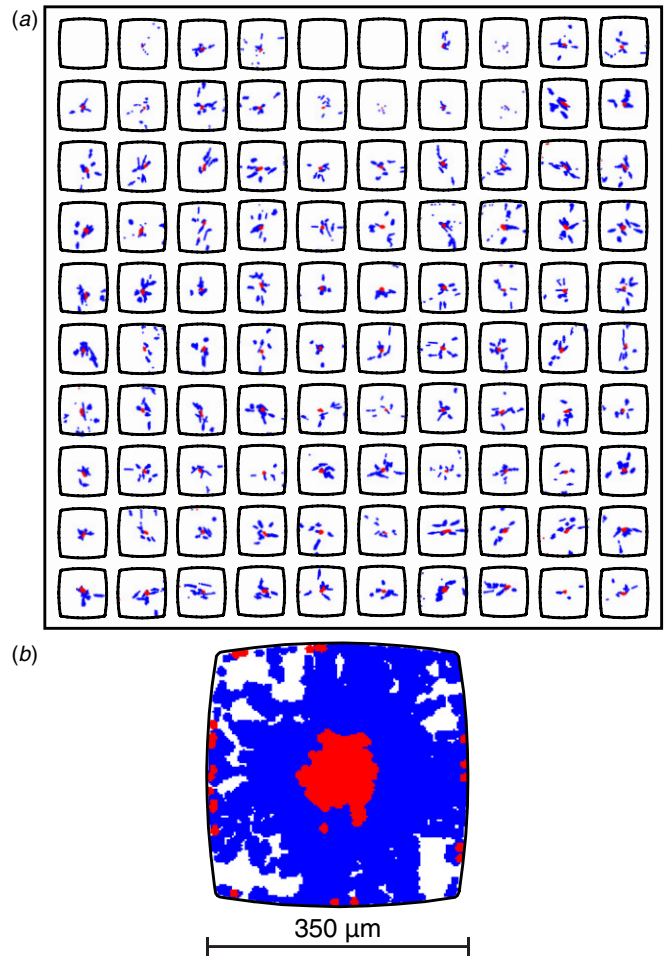


Figure 3. (a) Trapping result with 10 μm sized tracer particles in all 100 wells for frequency-modulation (FM) actuation ($2.30 \text{ MHz} \pm 100 \text{ kHz}$ @ 1 kHz, red) and for different single-frequency (SF) actuations (2.20, 2.23, 2.26, 2.29, 2.30, 2.33, 2.36, 2.39 and 2.40 MHz, blue). (b) Superposition of all 100 wells in (a) showing the overall effect of FM (red) and SF (blue) ultrasonic actuations.

several hundreds of kHz, which is needed for the particle manipulation experiments described below.

4.2. Positioning performance

The typical effect of SF versus FM actuation at 50 V_{pp} of a 10 μm particle sample for 2 min is visualized in figures 3(a)–(b). Here, approximately 900 beads are distributed in the 100 wells. As can be seen in figure 3(a), which is a superposition of nine different SF and FM actuations (data from in total 1000 wells: $(9 + 1) \times 100$), the stable positions of the clusters deviate significantly from the 100-well centers at SF actuation (blue clusters), while the corresponding positions at FM actuation are closer to the well centers (red clusters). Furthermore, the clusters are more confined and compact at FM actuation compared to the more elongated and sometimes fragmented clusters at SF actuation. The overall positioning accuracy is visualized in figure 3(b), where all 1000 wells in figure 3(a) are superimposed. As can be seen in figure 3(b), the applied voltage in this experiment was not enough to drive the particles into contact with the walls from the well centers.

There are about 20 out of 900 particles stuck at the wall when applying FM actuation, corresponding to approximately 2%.

In order to quantify the positioning accuracy of few-particle clusters, two different figures of merit were used: distance from the cluster center to the well center (figure 4(a)), and size of the well-centered minimum area covering all clusters (figures 4(b)–(j)). In these experiments, we analyzed data from nine different single actuation frequencies and compared them with FM actuation. This was performed in all the 100 wells, thus, in total data from $(9 + 1) \times 100 = 1000$ wells. The analyzed SFs were selected within the bandwidth of the FM actuation and symmetrically around the center frequency. In the first figure of merit, the distance from the center of the well to the center of mass for each cluster was calculated for both SF and FM actuations. For the analyzed dataset, this distance decreased from $71 \mu\text{m} \pm 49 \mu\text{m}$ for the SF actuations to $16 \mu\text{m} \pm 11 \mu\text{m}$ for FM actuation, thus, a factor 4 times better positioning accuracy for FM actuation relative to SF actuation. For the second figure of merit, the minimum well-centered area covering all clusters for both SF and FM actuations was measured by calculating the contours of the clusters processed from binary images of 100 superimposed wells. This figure of merit can be used for estimating the minimum FOV needed to cover the cluster in a high-resolution confocal-microscopy scan. Comparing SF with FM actuation, we see that the FOV area for FM actuation is merely 15% of the corresponding FOV area for SF actuation. Thus, we expect a similar reduction in scanning time for high-resolution confocal-microscopy imaging of the cluster for FM actuation relative to SF actuation. Finally, as seen in figure 5, the average cluster position in all of the 100 wells for the nine different SFs coincides relatively well with the average position for FM actuation: the distance between the average position of all nine different SFs and the average position for FM is approximately $6 \mu\text{m}$ (data from 1000 wells). This is expected since FM is in fact a time-average of all SF-generated force fields within the modulation band. This time-averaged actuation effect causes a similar position-averaged effect of the particle clusters, given that the modulation frequency is fast enough to prevent the particles moving between the different trapping positions of the SF fields within the modulation band [31]. However, it is interesting to see that the trapping position for FM actuation is closer to the well center than the average position of the nine selected SFs within the FM band. We believe this is because there exist more than 9 resonance frequencies within the FM band, and/or that the force magnitudes are different for the different selected SFs. Thus, the complex resonant behavior of the multiwell plate is important for the successful positioning performance of FM actuation, which is confirmed by the results in figures 4 and 5.

4.3. Quantification of acoustic forces, pressures, energy densities and acoustic streaming

In order to estimate the acoustic forces, pressures and energy densities in the 100-well plate, we studied the transient migration of $10 \mu\text{m}$ particles directly after the transducer was

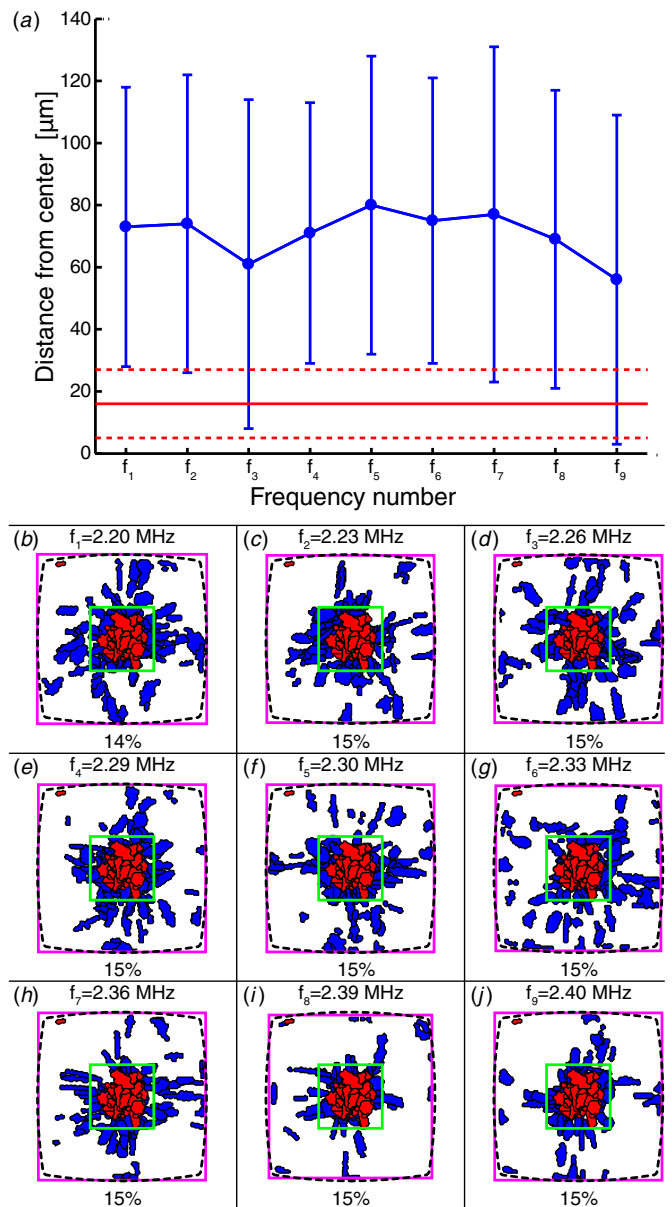


Figure 4. (a) Distances from the center of the well to the center of the clusters for single-frequency (SF) actuations ($f_1, \dots, f_9 = 2.20, 2.23, 2.26, 2.29, 2.30, 2.33, 2.36, 2.39$ and 2.40 MHz, blue) and frequency-modulation (FM) actuation ($2.30 \text{ MHz} \pm 100 \text{ kHz}$ @ 1 kHz , red). Here vertical error bars (blue) and horizontal dashed lines (red) indicate the standard deviations, and the solid line (red) and filled blue circles mark the average distances. (b)–(j) Positioning accuracy as a function of field of view (FOV) for SF actuation (f_1, \dots, f_9 , blue clusters) and for FM actuation ($2.30 \text{ MHz} \pm 100 \text{ kHz}$ @ 1 kHz , red clusters). For each frequency, f_1 through f_9 , the result from all wells are superimposed into a single well. The two squares for each frequency indicate the minimum well-centered FOV needed to cover all clusters under FM actuation (green) and SF actuation (magenta). Under each well the FOV ratio for FM and SF actuation is given in per cent. Here empty wells (i.e. containing no beads) and wells with single beads are removed since in our intended application we are only interested in cell aggregates of a minimum of two cells. Furthermore, the cluster close to the wall (red cluster in upper left corner) for FM actuation is disregarded as this cluster got stuck to the wall in one of the 100 wells and clearly is not an effect of the frequency modulated ultrasound actuation.

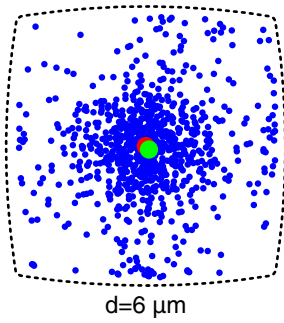


Figure 5. Positioning performance in all wells in the 100-well microplate as a function of frequency actuation scheme, i.e. frequency-modulation (FM) actuation and single-frequency (SF) actuation. All 100 wells are superimposed into a single well for FM and SF, i.e. data from 1000 wells. The same well selection criterion as used in figure 4 was implemented here. The distance, d , under the well is the measured distance between the average center of the bead clusters under FM actuation ($2.30 \text{ MHz} \pm 100 \text{ kHz}$ @ 1 kHz , red circle) and the average center under SF actuation ($2.20, 2.23, 2.26, 2.29, 2.30, 2.33, 2.36, 2.39$ and 2.40 MHz , green circle). To emphasize, blue dots indicate the center of individual bead clusters for the nine different SFs, and the green circle is the average center of all blue dots.

turned on at a high voltage ($U_{pp} = 210 \text{ V}$ corresponding to an average power of $\sim 6 \text{ W}$). This was performed by tracking the particle position as a function of time, from which the mean and maximum particle speeds were calculated using the Tracker software. Figure 6(a) displays the tracks of 33 individual particles, taken from 6 repetitions in one of the wells (including sample refilling between each repetition). Overlaid on these $10 \mu\text{m}$ particle tracks, figure 6(a) also displays average truncated μPIV plots (based on the motion of $1 \mu\text{m}$ particles) representing the average acoustic streaming field during the first 0.5 s after the transducer is turned on. From the six repetitions, the maximum acoustic streaming close to the bottom of the well was $17 \mu\text{m s}^{-1} \pm 11 \mu\text{m s}^{-1}$. The average time for trapping 30 out of 33 ($10 \mu\text{m}$ sized) particles into the calculated FOV (see green squares in figure 2) during FM actuation was measured to be $2.6 \text{ s} \pm 1.6 \text{ s}$; here, three particles are excluded since they started inside the FOV. The average speed of the particles when migrating toward the trapping site was measured to be $100 \mu\text{m s}^{-1} \pm 49 \mu\text{m s}^{-1}$ and the maximum speed to be $132 \mu\text{m s}^{-1} \pm 55 \mu\text{m s}^{-1}$. Via equations (3a), (3b) and (4), the maximum particle speed was then used for calculating the maximum acoustic energy density, the maximum acoustic radiation force and maximum acoustic pressure, see figure 6(b). Typically, the acoustic energy density ranges from 1 to 4 J m^{-3} , and the acoustic radiation force on the $10 \mu\text{m}$ particles ranges from 10 to 50 pN . This corresponds to pressure amplitudes of $0.3\text{--}0.7 \text{ MPa}$. We believe that the upper values are the most representative for estimating the acoustic force magnitudes, while the lower values are caused by the influence from other forces, e.g. particle–surface interactions. Furthermore, it is interesting to note that although the final trapping location is very close to the well center for all repetitions, the individual paths from particles initially located at the same part of the well differ significantly. We believe this effect is attributed to particle–particle and/or particle–wall

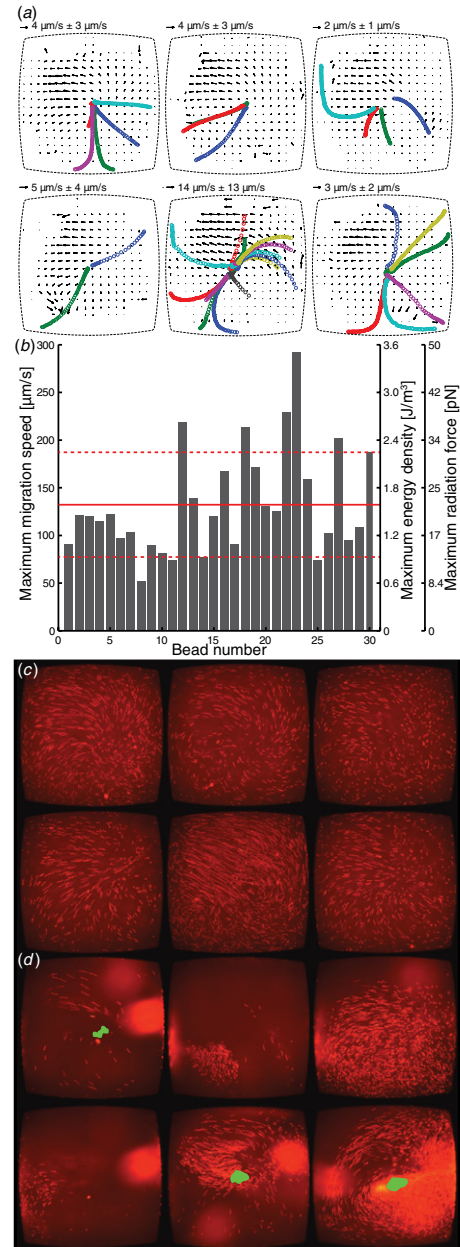


Figure 6. (a) Particle tracking of $10 \mu\text{m}$ particles overlaid on average truncated μPIV plots of $1 \mu\text{m}$ particles for the first ten frames of 0.5 s initial trapping for the same well under the same conditions for 6 repetitions under frequency-modulation actuation ($2.36 \text{ MHz} \pm 100 \text{ kHz}$ @ 1 kHz). The arrow above each μPIV plot indicates the average acoustic streaming speed. (b) Maximum migration speed of the $10 \mu\text{m}$ particles and their corresponding energy densities as well as radiation forces. The maximum migration speed is measured during the migration from the particles initial starting position and until they reach the minimum FOV (well-centered square with an area covering approx. 15% of the full well area) calculated in figures 4(b)–(j), green square. The red solid line shows the average maximum migration speed with the standard deviation marked as red dashed lines. (c) The initial and (d) final acoustic streaming patterns in the same well are shown by overlays made from the first and last ten frames (0.5 s) for each of the six repetitions. The large red areas in (d) are clusters of $1 \mu\text{m}$ sized tracer particles slowly being aggregated during the experiments. Green areas in (d) mark the final cluster position in the wells.

interactions. Finally, it should be noted that acoustic streaming along the symmetry axis of the wells sometimes caused the trapped particles to escape vertically for the high actuation voltage used (210 V), see figure 6(d). Therefore, we suggest lowering the actuation voltage after the completion of trapping for long-term positioning applications.

4.4. Robustness and time dependence of the acoustic streaming

The robustness and time dependence of the acoustic streaming was measured during 5 min of continuous high-voltage ($U_{pp} = 210$ V corresponding to an average power of ~ 6 W) ultrasonic actuation of the device. One important parameter that may influence the acoustic trapping and streaming performance is the temperature [32, 33]. For that reason, the surface temperature on the PZT piezo crystal and the ambient air temperature in the close vicinity of the device were measured every second. In figure 7(a), we plotted the temperature on the piezo crystal compensated for the slow air temperature drift ($1.4^\circ\text{C} \pm 0.4^\circ\text{C}$ over 3 h of monitoring), which affected the starting temperature for each repetition. Furthermore, it should be noted that we did not measure directly the fluid temperature during the particle manipulation experiments. Instead, we measured it separately by monitoring the fluid temperature with a temperature probe placed in the fluid through a drilled hole in the center of the cover glass, cf figure 1. This temperature was $0.7^\circ\text{C} \pm 0.4^\circ\text{C}$ lower than the piezo crystal surface temperature.

Interestingly, as the piezo crystal temperature increased from the (ambient-air-compensated) initial temperature around 24.8°C to a near-steady state around 34.6°C , the average acoustic streaming speed varied greatly as can be seen from figure 7(b). The streaming speed was calculated from μPIV analysis of the region of interest marked in figures 7(c)–(h). This region was selected since particles were not completely depleted there during the 5 min of ultrasonic actuation. However, the large standard deviations seen in figure 7(b) are due to the complex behavior of the acoustic streaming on primarily the local concentration of the $1\ \mu\text{m}$ sized tracer particles: the μPIV algorithm yields higher standard deviations when the local particle concentration decreases and when the particle speed increases. Figures 7(c)–(h) support this hypothesis by showing the distribution of tracer particles in one of the wells as the experiment progresses. As can be seen, the even distribution of tracer particles at the start of actuation (figure 7(c)) is successively transformed into a heterogeneous distribution with depleted areas and large $1\ \mu\text{m}$ particle clusters positioned at the well walls, shown by the large red areas in figures 7(f)–(h). This clustering effect of the tracer particles influences the overall acoustic streaming behavior, which in turn influences the continued particle clustering. This explanation is further supported by the apparently chaotic process of $1\ \mu\text{m}$ particle clustering demonstrated in figures 7(c)–(d). Although the initial conditions for the six repetitions were as identical as possible, the final pattern of $1\ \mu\text{m}$ particles is very different in terms of clustering degree and cluster locations. Thus, care must be taken when

measuring acoustic streaming with high concentrations of tracking particles close to the threshold of the smallest particle possible to manipulate in an ultrasonic standing wave. For our employed frequency of around 2.3 MHz, this threshold diameter is approximately $1.3\ \mu\text{m}$ [27].

Another important parameter that may influence the trapping and streaming performance is the fluid volume stored in and above the wells. This volume not only affects directly the acoustic energy density stored in the device but also the acoustic resonance in the whole system. We performed measurements where the acoustic streaming close to the bottom of a well was monitored while changing the fluid volume from 15 to 50 μL in steps of 5 μL . In this experiment, we tuned the driving voltage until we reached the physiological temperature of 37°C on the piezo surface, in order to simulate realistic conditions for the aimed bio-application. The acoustic streaming was then analyzed using μPIV , see figure 8. In general, the fluid volume has little effect on the overall acoustic streaming when driving the device with frequency-modulated actuation. On average the acoustic streaming speed is $4.6\ \mu\text{m s}^{-1} \pm 3.0\ \mu\text{m s}^{-1}$ for fluid volumes ranging from 15 to 50 μL . This streaming speed is well below reported levels that may cause shear-stress-induced cell damage [17].

5. Discussion and conclusion

The aim of the current study is to characterize and quantify the performance of ultrasound-mediated aggregation and positioning of cells in a 100-well microplate. This method can be used for detailed optical characterization of time-dependent cellular properties, including cell–cell interactions [12]. For such applications, it is beneficial that the time for the cell positioning and aggregation of the ultrasonic method is minimized, and that the temporal resolution of the confocal-microscopy screening time is improved.

We have shown in this paper that the positioning and aggregation time can be lowered from minutes [12] to a few seconds by the use of a ring transducer instead of the previously used wedge transducer. However, these measurements were performed on polystyrene particles. Since our described method is designed for cellular applications, it is of interest to estimate the trapping performance of cells based on our measured trapping results with particles. According to equations (1a)–(1d), the acoustic radiation force in an acoustic field of a given energy density E_{ac} is proportional to the acoustic contrast factor, Φ . This factor is dependent on the difference in density and compressibility of the particle, relative to its suspension medium (typically water). For polystyrene, these material properties are constant and well known. For cells, on the other hand, equations (1a)–(1d) can only be used for order-of-magnitude estimations since they are defined for homogeneous and spherical particles (which is not the case for cells). This also means that the contrast factor Φ can only be determined empirically. One example of such a study is that by Barnkob *et al* [34] who found that for white blood cells, Φ was roughly 3–10 times smaller than that of polystyrene. Another example is the study by Hartono *et al* [35] who used a similar approach and found that the contrast

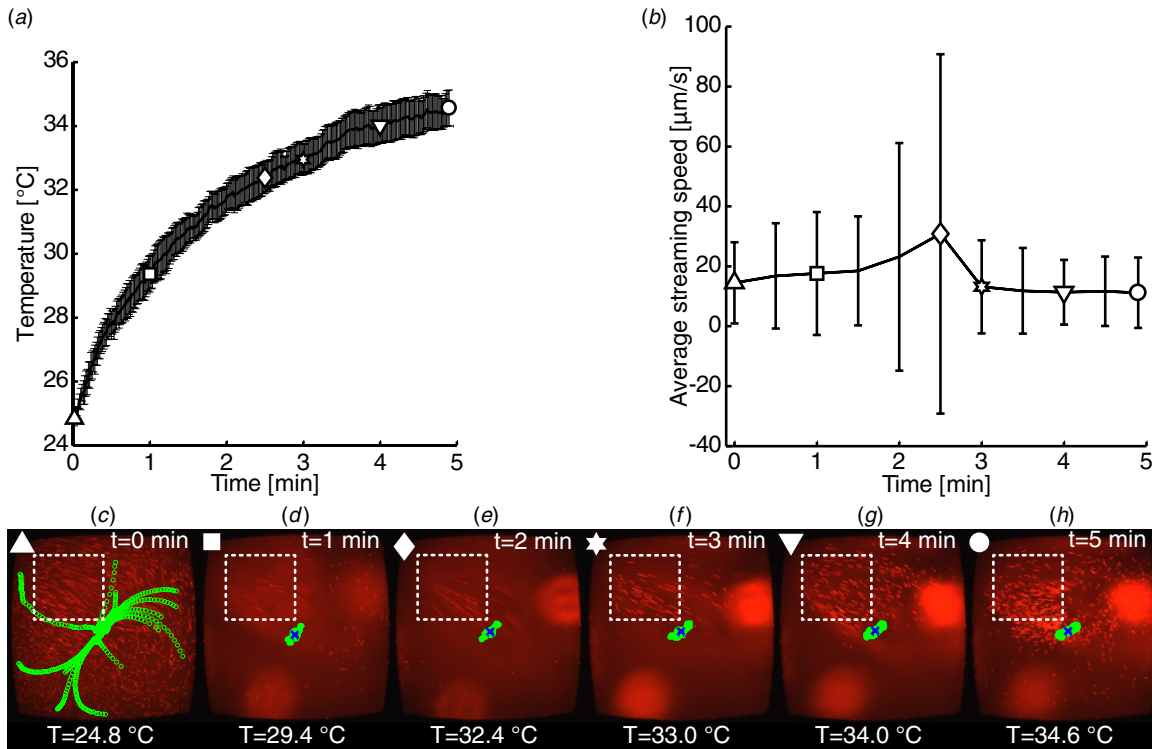


Figure 7. Time dependence of the acoustic streaming speed under frequency-modulation actuation ($2.36 \text{ MHz} \pm 100 \text{ kHz} @ 1 \text{ kHz}$), compared with the temperature increase. (a) The PZT piezo surface temperature adjusted for air temperature fluctuations during the 5 min long experiment for the same well under the same conditions for six repetitions. The black solid line shows the average adjusted temperature on the surface with standard deviations shown as gray-colored error bars. (b) Average acoustic streaming speed of $1 \mu\text{m}$ particles measured by average truncated μPIV . (c)–(h) Frames from repetition 5 (cf mid lower image in figures 6(c) and (d) showing the acoustic streaming for the six individual time points (indicated by the six symbols in plots (a) and (b)) and their corresponding temperatures. White dashed boxes show the region of interest for which the average streaming speed was calculated using average truncated μPIV analysis of 10 frames for every 30 s, i.e. 11 data points for 5 min. The box was placed in the location of maximum acoustic streaming in each of the six repetitions. The particle and cluster positions in (c)–(h) are indicated by green color with the center of mass marked with blue crosses in (d)–(h).

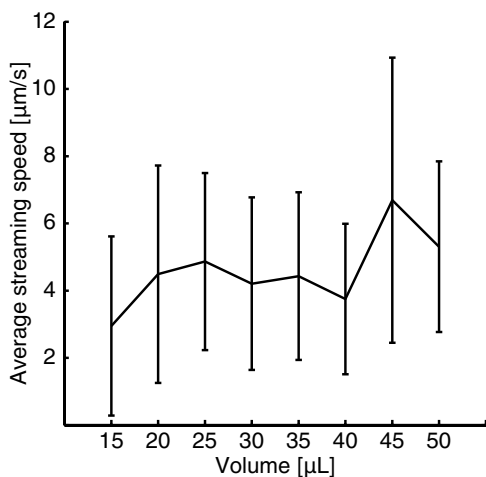


Figure 8. The average acoustic streaming speed at the bottom of a well as a function of the total fluid volume above and in the wells. Here vertical lines represent standard deviation. The experiment was repeated 10 times in the same well generating in total 32 000 images. μPIV analysis was performed for all images in a region of interest covering approx. 12% of the total well bottom area in order to minimize the influence of local particle depletion. Throughout the repetitions, the temperature on the piezo was kept at $36.9 \text{ }^\circ\text{C} \pm 0.4 \text{ }^\circ\text{C}$.

factor for red blood cells was 1.5 times smaller than that for polystyrene, and for different types of cancer cells 2–4 times smaller than that of polystyrene. Furthermore, Mishra *et al* [36] concluded from numerical modeling that for biological cells, the contrast factor was less dependent on shape but more dependent on internal structures/inhomogeneities. For example, the force on a cell with nucleus was predicted to be approx. twice the force of a non-nucleated cell of similar size. In summary, we may expect the acoustic radiation force in a given acoustic field to be roughly a few times lower on cells than on polystyrene particles of similar size, and the corresponding trapping time is expected to be a few times longer. Thus, our measured average trapping time of $2.6 \text{ s} \pm 1.6 \text{ s}$ for $10 \mu\text{m}$ polystyrene particles translates to about one or a few tens of seconds for cells.

Although we may position and aggregate particles within seconds by the use of the ring transducer, there are other problems introduced at these high voltages ($\sim 100\text{--}200 \text{ V}$). In this paper, we studied two such effects: temperature and acoustic streaming. A change in temperature is known to affect the acoustic resonances and may lead to decreased efficiency of acoustic particle manipulation [37]. For the resonance built up in the chip, the effect of changing the temperature is similar to the effect of changing the actuation

frequency. On the other hand, our actuation method based on frequency modulation (FM) has the additional advantage of minimizing the effect of temperature changes on the particle manipulation performance. For example, we did not observe any noticeable drift in the trapping position of 10 μm particles at FM actuation when the temperature increased to 10 $^{\circ}\text{C}$ (cf figures 7(c)–(h)). On the other hand, we did observe in some wells of the microplate that trapped particles escaped from the trapping position due to acoustic streaming at high-voltage actuation. This happened in three out of six repetitions in figures 6(c)–(d). Typically, the direction of escape is upward from the center position at the bottom of the wells. However, the escaped particles may be re-trapped by simply lowering the transducer voltage. Therefore, we suggest that the optimal actuation scheme is to turn on the transducer at around $U_{\text{pp}} = 200$ V for a few seconds and then decrease the voltage to 50 V. This makes the transient trapping process efficient and the prolonged positioning stable.

Temperature control has been used for stabilizing acoustic particle trapping [37], but this method has not been evaluated yet for stabilization of acoustic streaming. This may be a successful method for our device, in particular since it also causes improved biocompatibility of the method [17]. It should be noted, though, that we do not know to what extent the chaotic variations in acoustic streaming over time depend on clustering effects of the 1 μm tracer particles on the temperature variations or on fluid volume changes. This will be investigated in the future by upgrading our device with a Peltier cooler element [17]. One argument that supports our hypothesis that temperature control may be important for controlling acoustic streaming is that the acoustic streaming is strongly dependent on the viscosity (which in turn is temperature dependent) [32]. The viscosity is not an important parameter for the acoustic radiation force on polymer particles in water [33], which may explain why our FM method is sufficient for stabilizing the particle trapping without any temperature control.

It is interesting to compare the performance of the ring transducer with the performance of our previously used wedge transducer [8, 18]. There are two design criteria that need to be fulfilled: the transducer needs to be sufficiently broadband for matching the FM bandwidth, but still efficient in delivering acoustic energy into the wells without increasing the temperature of the device too much. In terms of bandwidth, the ring transducer and the wedge transducer have similar properties (i.e. broadband enough for the typical frequency sweeps used). However, the major advantage of the ring transducer compared with the wedge transducer is that the driving voltage can be much higher before reaching a critical temperature (which is the physiological temperature in our suggested bio-application). For example, figure 7 shows that the maximum temperature increase is of the order of 10 $^{\circ}\text{C}$ when driving the ring transducer at >200 V. The same temperature increase was reached at only 20 V driving voltage by the use of the wedge transducer [21], resulting in much slower particle aggregation. Thus, we may conclude that the ring transducer can be operated at higher voltages without reducing the biocompatibility of the device. It should

be noted, however, that it is not the driving voltage itself that defines the biocompatibility, but rather the resulting temperature and acoustic pressure levels in the wells. These levels (cf figure 6(b)) are below reported levels of safe, long-term ultrasonic manipulation [17]. Finally, it should be noted that both the ring transducer and the wedge transducer designs differ from the conventional transducer design used for ultrasonic particle manipulation. Most other reports in the literature describe high- Q frequency-specific resonators [38, 39], while our approach is to use lower- Q and slightly broadband transducers compatible with our FM approach. On the other hand, neither low- Q nor ring transducers are novel for ultrasonic particle manipulation. For example, Wiklund *et al* have demonstrated a glue-backed ring transducer for the coupling of a standing wave into a narrow-bore fused silica capillary [40, 41].

We have previously demonstrated how the ultrasonic method can be used for high-resolution imaging of the immune synapse formed between a NK cell and a cancer cell [11]. The imaging was performed by a 3D confocal-microscopy volume scan, which unfortunately is a slow imaging technique. Therefore it is crucial to limit the field of view (FOV) of each scan, which in turn requires that the imaged cell aggregate is fixed in position during the full time of examination. In this paper, we have quantified the positioning accuracy and estimated the smallest pre-defined FOV compatible with our device. Typically, this FOV is approximately 15% of the full well area when operating our device with frequency-modulated actuation (cf figure 4), but this percentage is dependent on the number of cells in the aggregate. In the future, our results in this paper can be used for calibrating an automatic time-lapse scanning procedure for confocal microscopy where only the areas containing the trapped cell aggregates are imaged at high resolution.

Acknowledgments

The authors are grateful for financial support from the Swedish research council, grant no. 2011-5230, and the EU-FP7 project ‘RAPP-ID’ in the Innovative Medicines Initiative (IMI).

References

- [1] Coakley W T 1997 Ultrasonic separations in analytical biotechnology *Trends Biotechnol.* **15** 506–11
- [2] Bruus H, Dual J, Hawkes J, Hill M, Laurell T, Nilsson J, Radel S, Sadhal S and Wiklund M 2011 Forthcoming lab on a chip tutorial series on acoustofluidics: acoustofluidics-exploiting ultrasonic standing wave forces and acoustic streaming in microfluidic systems for cell and particle manipulation *Lab Chip* **11** 3579–80
- [3] Lenshof A, Magnusson C and Laurell T 2012 Acoustofluidics 8: applications of acoustophoresis in continuous flow microsystems *Lab Chip* **12** 1210–23
- [4] Yu G, Chen X L and Xu J 2011 Acoustophoresis in variously shaped liquid droplets *Soft Matter* **7** 10063–9
- [5] Lin S C, Mao X and Huang T J 2012 Surface acoustic wave (SAW) acoustophoresis: now and beyond *Lab Chip* **12** 2766–70
- [6] Nilsson J and Evander M 2012 Acoustofluidics 20: applications in acoustic trapping *Lab Chip* **12** 4667–76

- [7] Bruus H 2012 Acoustofluidics 7: the acoustic radiation force on small particles *Lab Chip* **12** 1014–21
- [8] Vanherberghen B, Manneberg O, Christakou A, Frisk T, Ohlin M, Hertz H M, Onfelt B and Wiklund M 2010 Ultrasound-controlled cell aggregation in a multi-well chip *Lab Chip* **10** 2727–32
- [9] Wiklund M, Green R and Ohlin M 2012 Acoustofluidics 14: applications of acoustic streaming in microfluidic devices *Lab Chip* **12** 2438–51
- [10] Ohlin M, Christakou A E, Frisk T, Önfelt B and Wiklund M 2011 *Proc. 15th Int. Conf. on Miniaturized Systems for Chemistry and Life Sciences (μTAS 2011) (Seattle, WA, USA, 2–6 Oct.)* pp 1612–4
- [11] Christakou A E, Ohlin M, Khorshidi M A, Frisk T, Vanherberghen B, Önfelt B and Wiklund M 2011 Aggregation and long-term positioning of cells by ultrasound in a multi-well microchip for high-resolution imaging of the natural killer cell immune synapse *Proc. 15th MicroTAS, (Seattle, WA, USA, 2–6 Oct.)* pp 329–31
- [12] Christakou A E, Ohlin M, Vanherberghen B, Khorshidi M A, Kadri N, Frisk T, Wiklund M and Önfelt B 2012 Quantification of natural killer cell cytotoxicity at the single cell level assisted by ultrasound mediated cell aggregation in multiwell microchips (submitted)
- [13] Lindström S and Andersson-Svahn H 2012 *Single-Cell Analysis: Methods and Protocols* vol 853 ed S Lindström and H Andersson-Svahn (Hatfield: Humana Press) pp 41–52
- [14] Voldman J, Gray M L, Toner M and Schmidt M A 2002 A microfabrication-based dynamic array cytometer *Anal. Chem.* **74** 3984–90
- [15] Guldevall K, Vanherberghen B, Frisk T, Hurtig J, Christakou A E, Manneberg O, Lindstrom S, Andersson-Svahn H, Wiklund M and Onfelt B 2010 Imaging immune surveillance of individual natural killer cells confined in microwell arrays *PLoS One* **5** e15453
- [16] Frisk T W, Khorshidi M A, Guldevall K, Vanherberghen B and Onfelt B 2011 A silicon-glass microwell platform for high-resolution imaging and high-content screening with single cell resolution *Biomed. Microdevices* **13** 683–93
- [17] Wiklund M 2012 Acoustofluidics 12: biocompatibility and cell viability in microfluidic acoustic resonators *Lab Chip* **12** 2018–28
- [18] Manneberg O, Svennebring J, Hertz H M and Wiklund M 2008 Wedge transducer design for two-dimensional ultrasonic manipulation in a microfluidic chip *J. Micromech. Microeng.* **18** 095025
- [19] Manneberg O, Vanherberghen B, Svennebring J, Hertz H M, Onfelt B and Wiklund M 2008 A three-dimensional ultrasonic cage for characterization of individual cells *Appl. Phys. Lett.* **93** 063901
- [20] Svennebring J, Manneberg O, Skafte-Pedersen P, Bruus H and Wiklund M 2009 Selective bioparticle retention and characterization in a chip-integrated confocal ultrasonic cavity *Biotechnol. Bioeng.* **103** 323–8
- [21] Svennebring J, Manneberg O and Wiklund M 2007 Temperature regulation during ultrasonic manipulation for long-term cell handling in a microfluidic chip *J. Micromech. Microeng.* **17** 2469–74
- [22] King L V 1934 On the acoustic radiation pressure on spheres *Proc. R. Soc. Lond. A* **147** 212–40
- [23] Gor'kov L P 1962 On the forces acting on a small particle in an acoustical field in an ideal fluid *Sov. Phys.—Dokl.* **6** 773–5
- [24] Barnkob R, Iranmanesh I, Wiklund M and Bruus H 2012 Measuring acoustic energy density in microchannel acoustophoresis using a simple and rapid light-intensity method *Lab Chip* **12** 2337–44
- [25] Barnkob R, Augustsson P, Laurell T and Bruus H 2010 Measuring the local pressure amplitude in microchannel acoustophoresis *Lab Chip* **10** 563–70
- [26] Wiklund M, Brismar H and Onfelt B 2012 Acoustofluidics 18: microscopy for acoustofluidic micro-devices *Lab Chip* **12** 3221–34
- [27] Barnkob R, Augustsson P, Laurell T and Bruus H 2012 Acoustic radiation- and streaming-induced microparticle velocities determined by microparticle image velocimetry in an ultrasound symmetry plane *Phys. Rev. E.* **86** 056307
- [28] Brown D Tracker 4.62, free video analysis and modeling tool for physics education 2012 <http://www.cabrillo.edu/~dbrown/tracker/>
- [29] Mori N and Chang K 2003 Introduction to MPiV User Reference Manual <http://www.oceanwave.jp/softwares/mpiv>
- [30] Manneberg O, Vanherberghen B, Onfelt B and Wiklund M 2009 Flow-free transport of cells in microchannels by frequency-modulated ultrasound *Lab Chip* **9** 833–7
- [31] Glynn-Jones P, Boltryk R J, Harris N R, Cranny A W J and Hill M 2010 Mode-switching: a new technique for electronically varying the agglomeration position in an acoustic particle manipulator *Ultrasonics* **50** 68–75
- [32] Rednikov A Y and Sadhal S S 2011 Acoustic/steady streaming from a motionless boundary and related phenomena: generalized treatment of the inner streaming and examples *J. Fluid Mech.* **667** 426–62
- [33] Settnes M and Bruus H 2012 Forces acting on a small particle in an acoustical field in a viscous fluid *Phys. Rev. E* **85** 016327
- [34] Barnkob R, Augustsson P, Magnusson C, Lilja H, Laurell T and Bruus H 2011 Measuring density and compressibility of white blood cells and prostate cancer cells by microchannel acoustophoresis *Proc. 15th MicroTAS (Seattle, WA, USA, 2–6 Oct.)* pp 127–9
- [35] Hartono D, Liu Y, Tan P L, Then X Y S, Yung L Y L and Lim K M 2011 On-chip measurements of cell compressibility via acoustic radiation *Lab Chip* **11** 4072–80
- [36] Mishra P, Glynn-Jones P, Boltryk R J and Hill M 2012 Efficient finite element modeling of acoustic radiation forces on inhomogeneous elastic particles *AIP Conf. Proc.* **1433** 753–6
- [37] Augustsson P, Barnkob R, Wereley S T, Bruus H and Laurell T 2011 Automated and temperature-controlled micro-PIV measurements enabling long-term-stable microchannel acoustophoresis characterization *Lab Chip* **11** 4152–64
- [38] Gröschl M 1998 Ultrasonic separation of suspended particles: part I. Fundamentals *Acoustica* **84** 432–47
- [39] Hill M 2003 The selection of layer thicknesses to control acoustic radiation force profiles in layered resonators *J. Acoust. Soc. Am.* **114** 2654–61
- [40] Wiklund M, Nilsson S and Hertz H M 2001 Ultrasonic trapping in capillaries for trace-amount biomedical analysis *J. Appl. Phys.* **90** 421–6
- [41] Wiklund M, Spiegel P, Nilsson S and Hertz H M 2003 Ultrasonic-trap-enhanced selectivity in capillary electrophoresis *Ultrasonics* **41** 329–33